Surface & Coatings Technology 204 (2009) 571–579

Contents lists available at ScienceDirect

Surface & Coatings Technology

journal homepage: www.elsevier.com/locate/surfcoat

Structural and electrochemical performance of sputtered Al–Ce films on AA6061 aluminum alloy substrates

M.A. Domínguez-Crespo [a,*], S.E. Rodil [b], A.M. Torres-Huerta [a], E. Ramírez-Meneses [a], G. Suárez-Velázquez [c]

[a] Instituto Politécnico Nacional, CICATA-Unidad Altamira-Tamaulipas, km 14.5, Carretera Tampico-Puerto Industrial Altamira. C. P. 89600. Altamira, Tamps., Mexico
[b] Instituto de Investigación en Materiales, Universidad Nacional Autónoma de México, Circuito Exterior s/n, Ciudad Universitaria. Del. Coyoacán, C.P.04510 México D. F., Mexico
[c] Alumna del posgrado en Tecnología Avanzada. Instituto Politécnico Nacional, CICATA-Unidad Altamira-Tamaulipas, km 14.5, Carretera Tampico-Puerto Industrial Altamira. C. P. 89600. Altamira, Tamps., Mexico

A R T I C L E I N F O

Article history:
Received 8 June 2009
Accepted in revised form 26 August 2009
Available online 6 September 2009

Keywords:
DC magnetron sputtering
AA6061 aluminium alloy
Cerium oxides
Microstructure
Process parameters

A B S T R A C T

In this work, sputtered Al–Ce films were studied in order to evaluate their possible application as coatings to delay pitting corrosion of aluminum alloy substrates. The morphology and structure of the coatings deposited on both silicon and AA6061 aluminum alloy substrates were studied by varying the magnetron sputtering conditions. The preliminary electrochemical performance was also discussed by means of Tafel plots and electrochemical impedance spectroscopy (EIS). The X-ray diffraction studies indicated that the microstructure varied from crystalline to amorphous, depending on the deposition parameters. The AFM images show that the films consist of equi-axial round domes distributed homogeneously. The mean grain size, roughness and thickness of the coatings were increased by augmenting the power and pressure. The EIS studies showed that there was a significant increase in the resistance to corrosion after depositing Al–Ce films on AA6061 aluminum alloy substrates. The electrochemical behavior of the films was related to the Ce/Al composition ratio as well as process parameters.

© 2009 Elsevier B.V. All rights reserved.

1. Introduction

In recent years, the surface treatments or coatings with lanthanide salts have considerably progressed in order to replace highly toxic and carcinogenic chromate conversion coatings [1,2]. Cerium oxides have particularly raised much interest because of their good corrosion inhibition properties for aluminum, steel or magnesium [1,3,4]. These materials have been applied to: solid oxide fuel cells [5], corrosion and thermal barriers at high temperatures [6,7] and catalysts [8]. The wide variety of applications is due to their low toxicity; their ingestion or inhalation is not considered harmful to health [9]. They can successfully modify the surface of various metals and alloys because of their tendency to form oxides or hydroxides over cathodic zones, which has a blocking effect [10]. A good way to cope with corrosion problems is the application of thin films and protective coatings. Surface treatments and coatings applied onto aluminum and its alloys are of particular interest to prevent the degradation process; they represent a major field in industrial finishing due to their applicability to various fields, from the construction industry to electronics, aeronautics or automotive industries. The techniques for the application of lanthanide-based treatments to the anticorrosive protection of these aluminum alloys are various: sol–gel method [11], anodizing [12,13], chemical conversion coatings [7,14–16] and physical vapor deposition techniques [17,18]. Sputtering could be considered an emerging environmentally-friendly technology for the production of corrosion and wear-resistant coatings on light metals. Due to the possibility of a large deposition area, the high quality of the coatings and the ability to vary film properties in a controlled way, this technique appears to be one of the most interesting methods for commercial production [19,20]. However, it has been poorly investigated by scientists in the corrosion field. In this paper, the deposition and structural characterization of sputtered Al–Ce thin films on AA6061 aluminum alloys and suitable experimental conditions are discussed. The main aim of this work is to establish the relationship between the microstructure of the Al–Ce thin films and the corrosion mitigation effects on aluminum alloys.

2. Experimental

2.1. Film deposition

Aluminum AA6061 (disc form) samples were polished up to 600 grade SiC paper and cleaned with water and ethanol in an ultrasonic bath for 20 min before processing. The specimens selected for coating, structural characterization and electrochemical corrosion tests had a diameter of 0.025 m and a thickness of 0.002 m. Aluminum-based coatings were deposited by a commercial pulsed DC magnetron sputtering apparatus from a multicomponent target consisting of Al (99.95% purity, diameter of 0.1 m and thickness of 0.003 m) and eight Ce pieces (99.5% purity, 0.015 m × 0.005 m × 0.001 m) attached to

* Corresponding author.
E-mail addresses: mdominguezc@ipn.mx, adcrespo2000@yahoo.com.mx (M.A. Domínguez-Crespo).

0257-8972/$ – see front matter © 2009 Elsevier B.V. All rights reserved.
doi:10.1016/j.surfcoat.2009.08.041

Table 1
Deposition parameters and Correlation between the compositions obtained from EDS and RBS tecniques.

Experiment	Presure (Pa)	Power (W)	Thickness (nm)	Deposition rate (nm s^{-1})	Roughness (picometer)	Al/Ce ratio (EDS)	Oxygen at.% (RBS)	Al/Ce ratio (RBS)
$p_{0.667}P_{200}t_{300}$	6.66E−1	200	262.4	0.87467	576.87	0.0683	9.20	0.110
$p_{1.333}P_{200}t_{300}$	1.34	200	511.1	1.70368	705.65	0.1606	–	–
$p_4P_{200}t_{300}$	4.0	200	1214.5	4.04833	2104.10	0.6028	15.80	0.600
$p_4P_{280}t_{300}$	4.0	280	1171.7	3.90567	2238.02	0.4720	8.00	0.450
$p_4P_{120}t_{300}$	4.0	120	524.1	1.74713	1907.50	0.1761	40.00	0.375
$p_4P_{40}t_{300}$	4.0	40	102.2	0.34067	676.52	0.0101	–	–

the Al target race track. The vacuum chamber was initially pumped to a base pressure of $1.33*10^{-4}$ Pa. The deposition was done using an Ar (99.99% purity) atmosphere at flow rates between $1*10^{-5}$ and $1.4*10^{-5}$ scm. To study the effects of pressure and applied power on the film composition and corrosion behavior, two experiment sets were carried out. In the first set, the pressure was varied from $6.67*10^{-1}$ to 4 Pa at 200 W (namely $p_{0.667}P_{200}t_{300}$, $p_{1.333}P_{200}t_{300}$ and $p_4P_{200}t_{300}$); in the second set, the power was varied from 40 to 280 W at a constant pressure of 4 Pa ($p_4P_{40}t_{300}$, $p_4P_{120}t_{300}$ and $p_4P_{280}t_{300}$). The other deposition parameters were kept constant: the substrate was ground without bias, the substrate temperature was not controlled, but previous studies have shown that the maximum temperature reached at the substrate holder was ~80 °C, the deposition time was 300 s and the substrate-to-target distance (ds–t) was fixed at 0.050 m [21].

2.2. Structural and morphological characterization of the films

The coatings were simultaneously deposited onto two substrate materials that were chosen for their suitability for the particular analysis techniques: the samples deposited on silicon (111) were used for structural and morphological characterizations: X-ray diffraction (XRD), atomic force microscopy (AFM), scanning electron microscopy (SEM) and high resolution transmission electron microscopy (HRTEM); and thickness measurements by profilometry and SEM. The elemental composition of the films was obtained by both energy dispersive spectroscopy (EDS) and Rutherford backscattering (RBS) using a pelletron accelerator with a 2 MeV $^4He^{2+}$ particle beam and a scattering angle of 167° in the laboratory frame. The spectra simulation was performed with code SIMRA [21]. The XRD patterns of the films were obtained by using a Brucker D8 series diffractometer, with Cu Kα (λ = 0.154 nm) radiation, while atomic force microscopy (AFM) studies were carried out in a Nanosurf easyscan 2.0 microscope. The morphological aspects of the coatings were studied by scanning electron microscopy (SEM) using a JEOL JSM-35C. HRTEM studies were carried out on a JEOL 2010 FasTem field emission transmission electron microscope with a resolution of 2.1 Å.

2.3. Corrosion properties of the coatings

The corrosion behavior of the coated and uncoated alloys was determined by electrochemical impedance spectroscopy measurements. A potentiostat/galvanostat (Gamry 600 series), using a graphite bar as the counter electrode and a saturated calomel electrode (SCE) as the reference electrode, was employed to perform the corrosion experiments. The electrochemical cell consisted of an acrylic rectangular box (0.06×0.08×0.1 m), and the exposed area of the sample was $1.23*10^{-4}$ m^2. The front surfaces of the specimens were held in the cell by moderate pressure against an o-ring, avoiding localized damage to the films. The Tafel polarisation curves were measured from the

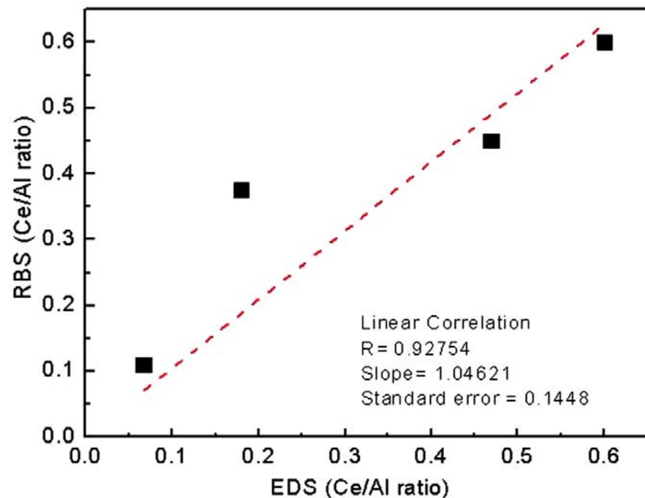

Fig. 1. Correlation between EDS and RBS.

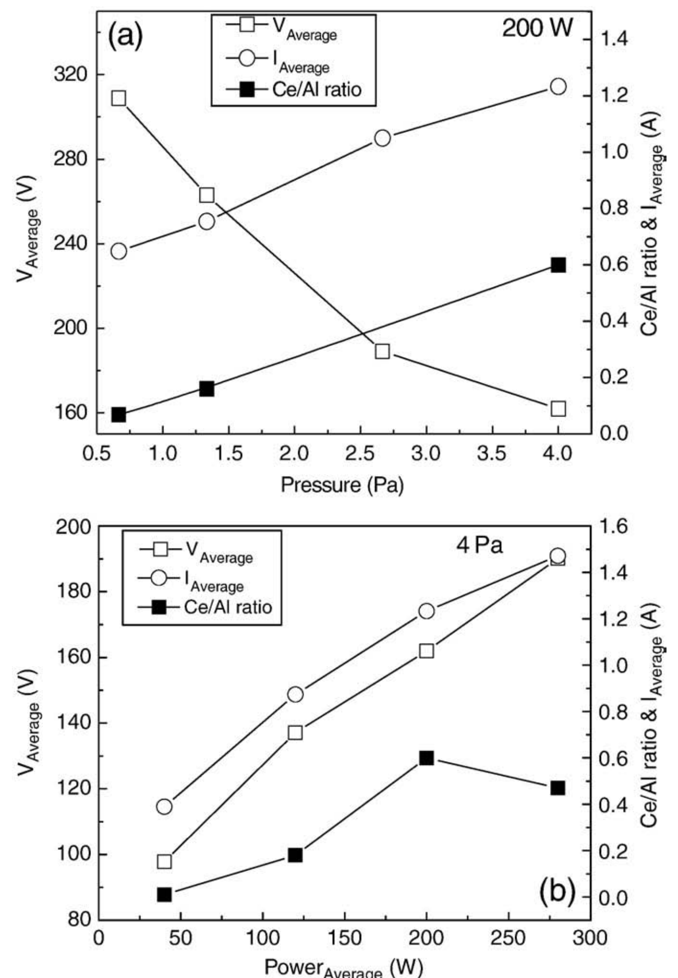

Fig. 2. Variation of both the voltage and current during deposition as a function of the experimental parameters a) pressure and b) power.

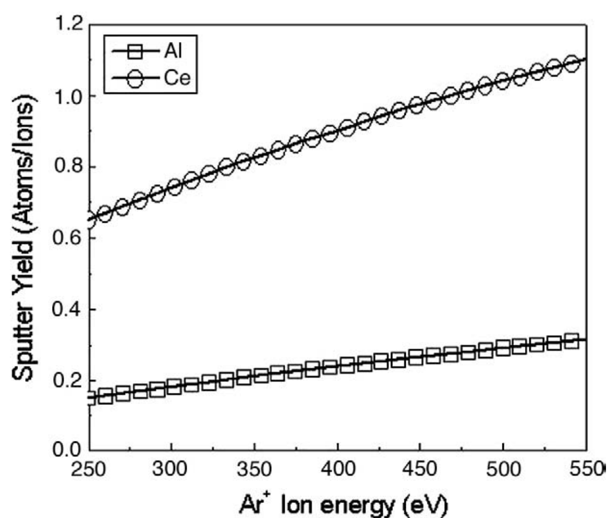

Fig. 3. Sputter yield calculated for a pure Ce and a pure Al target as a function of the Ar ion energy.

cathodic to anodic area. The scans were started at −250 mV *vs* SCE with a sweep rate of 1 mV s^{-1}, while the EIS measurements were carried out in the frequency region from 100,000 to 0.01 Hz (ten frequency points per decade) with an amplitude of 10 mV rms.

3. Results and discussion

3.1. Influence of the process parameters (power and pressure)

It is well known that the major steps of the coating process are the pretreatment of the alloy surfaces prior to coating, coating deposition parameters and treatment of the coated surfaces after deposition [22]. In order to evaluate the protection against corrosion given by the sputtered Al–Ce thin films, the substrates were polished up to 600 grade SiC paper, which is the standard surface finishing required by different ASTM standards [23]. The different experiments will be discussed in terms of the effect that the operating conditions exert on the composition (Ce/Al ratio), morphology, thickness and/or electrochemical performance of the Al–Ce coatings deposited by this technique. The deposition parameters used to obtain the Al–Ce layers with different compositions and thicknesses are listed in Table 1. The Ce/Al ratio was measured for all the samples by the EDS technique, but only selected samples were measured by RBS. The correlation between the obtained compositions and both techniques is shown in Fig. 1 and Table 1. The 1:1 correlation supported the data obtained by EDS. Fig. 2a–b shows the variation of both voltage and current during the deposition as functions of the experimental parameters: pressure (Fig. 2a) and power (Fig. 2b). The Ce/Al ratio measured by EDS is also included in both figures. Voltage and current are referred to as average values, since a pulsed DC source was used and the deposition was done at constant average power. From these figures, it can be seen that the Ce concentration follows the same trend as the current, except at the highest power (280 W). The highest Ce/Al ratio (0.6) was obtained for the sample deposited at 4 Pa and 200 W; the minimum value was for the 40-W sample. The latter could be a consequence of the surface binding energy of Ce (4.23 eV) which is higher than that of Al (3.36 eV), and limits the minimum energy to remove the Ce atoms from the target. The interesting point about this result is that the chosen deposition conditions exerted great influence on the Ce/Al ratio and, as a consequence, samples with marked differences could be evaluated.

This remarkable variation is partially consequence of the significant difference in the sputter yield of Ce in comparison to Al. Fig. 3 shows the sputter yield of Ce and Al calculated using the theoretical approximation proposed by Biersack and Eckstein [24], using the Monte Carlo program TRIM (Transport of Ions in Matter) [25]. This is a software package for computing the stopping range of ions in matter through a quantum mechanical treatment of ion–atom collisions. The determination of the sputtering yield in the incident energy range (250–550 eV) as a function of the incidence angle was also included. The marked difference in the sputter yield explains the efficient incorporation of Ce under certain conditions, but the low Ce contents are difficult to understand since the sputter yield calculation cannot be performed for very low Ar ion energies (equivalent to very low voltages). On the other hand, for the 280-W sample, where the voltage was high enough to expect remarkable differences between Ce and Al sputter yields (Fig. 3), there was a drop in the Ce incorporation. This was probably due to the same cause that induced a reduction in the deposition rate at the highest power. The deposition rate of the coatings also varied with the experimental conditions; we observed an increment in the deposition rate as the power was increased up to 200 W, and then a slight decrease from 4.04 to 3.90 nm s^{-1} was observed for the 280-W samples. This decrease in both the deposition rate and the Ce/Al ratio for the 280-W samples is not clear; re-sputtering or target poisoning are unlikely since no bias was used and the atmosphere was not reactive. Gas rarefication due to a higher amount of reactive Ce atoms in the gas could be proposed, although no drastic variation in the voltage–current characteristics were observed (Fig. 2b). This issue requires further experiments, which are beyond the objective of the present paper.

Finally, the increase in pressure had a beneficial effect on both the deposition rates and the Ce/Al ratio. This positive effect could be due to the highest target currents (Fig. 2a) that probably prompted a more effective sputter rate of the multi-component target.

3.2. Microstructural characterization

The X-ray diffraction patterns for the Al–Ce films deposited at different operating conditions are shown in Fig. 4. It was necessary to use different scales (usually 1:1.5) because the variation of the experimental conditions causes different intensities of the oxide compounds forming the film. It is worth mentioning that the oxygen contents obtained from RBS ranged from 8 to 40 at.%, Table 1. The base pressure in the vacuum chamber prior to the deposition of the films was good enough to avoid such a high oxygen contamination. However, it is well known that both Ce and Al are very reactive under environmental conditions; thus, it is very likely that the oxides were formed once the samples were exposed to the atmosphere. Some crystalline compounds

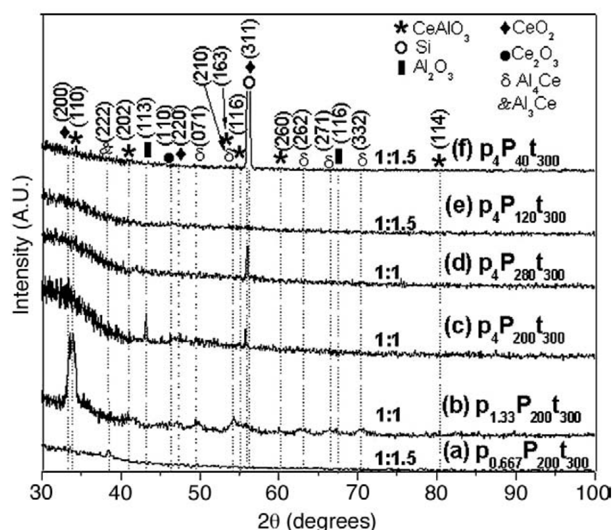

Fig. 4. X-ray diffraction patterns of Al–Ce coatings varying (a–c) pressure from 0.667 to 4 Pa (at 200 W) and (d–f) power from 40 to 280 W (at 4 Pa).

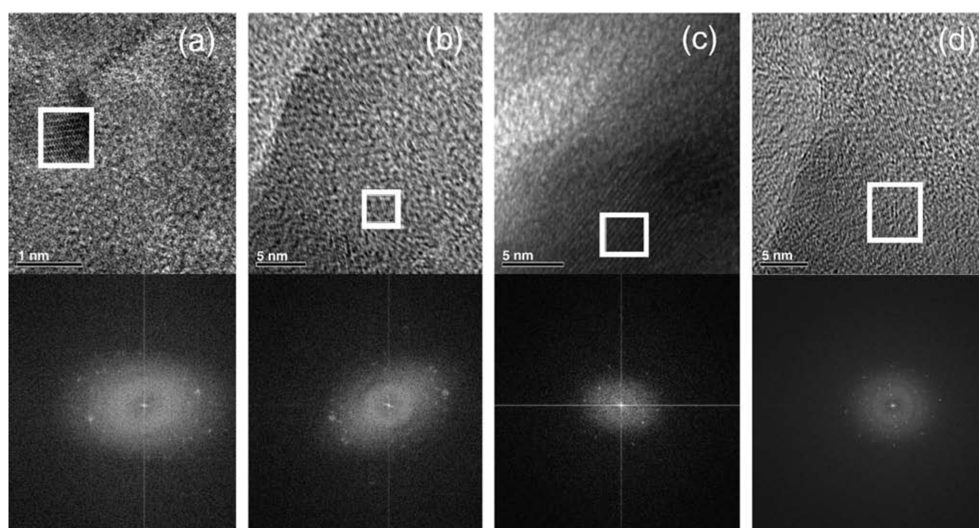

Fig. 5. HRTEM photographs of nanostructure and corresponding selected area electron diffraction of Al–Ce oxide films prepared at various process conditions (power and pressure): a) $p_4P_{280}t_{300}$, b) $p_4P_{200}t_{300}$, c) $p_4P_{40}t_{300}$ and d) $p_{1.333}P_{200}t_{300}$.

with low intensities can be observed as the pressure increases (at 200 W): $CeAlO_3$ (110) (202) (113) (116) (260) (114); Al_4Ce (0710), (210), (262), (271), (332); Al_3Ce (222), and CeO_2 (200), (220) (311). Additionally, the peaks around 55.7°, 43.19° and 46.2° belong to the Si (111) substrate, in the oriented reflection (311), underneath the film, the presence of aluminum oxide (Al_2O_3), and cerium oxide (Ce_2O_3), respectively. On the other hand, amorphous coatings were obtained at low and medium power, Fig. 4(e–f), maintaining constant pressure (at 4 Pa); while at high powers some crystalline compounds could be detected (Fig. 4c–d). Then, nanocrystalline structures in the coatings are only seen at high power and low pressure. The structural characterization of the films on the aluminum alloy (not shown here) displayed unchanged reflections, which suggests that the substrate did not have any influence on either the grade of crystallinity or orientation during the growth of the film. It is very interesting that the aluminum films that were oxidized under environmental conditions (Al_2O_3) and synthesized at the experimental conditions showed nanocrystalline patterns. Due to the fact that the coatings depend on the amount and type of element added to a base, two groups of metallic films can be considered: a) the films of the first group, characterized by relatively narrow X-ray reflection lines (FWHM $<$ 1°); and b) films with very fine grained nanocrystals or amorphous films characterized by very broad low-intensity reflections (FWHM $>$ 1°) [26]. According to this classification, the as-deposited films belong to the last group, indicating that cerium is inhibiting the crystallization of Al_2O_3 in the film with some small crystals of metallic compounds embedded in the matrix. Determination of the useful impact of this amorphization for industrial applications is in progress. In order to confirm the microstructure of the samples, HRTEM micrographs of selected samples and the corresponding SAED are shown in Fig. 5a–d. These micrographs show a well-dispersed Al–Ce system with some crystallites embedded in a crack-free amorphous matrix, which is in agreement with the XRD results. The crystalline areas are clearly visible, but in some regions are diffused on the amorphous matrix. In general, the coating growth by the sputtering technique proceeds in three steps. The first step involves the transport of the coating species to the substrate; the second step is the adsorption of the species onto the surface of the substrate or growing coating, their diffusion over this surface, and finally either their incorporation into the coating or their removal from the surface by evaporation or sputtering. The third step consists of the movement of the coating atoms to their final position within the coating by processes such as bulk diffusion [27]. From the HRTEM results, it can be seen that pressure seems to exert great influence on the crystallinity of the films, which suggests that the growth of the film is likely affected in the microstructure by the pressure; i.e., the transport step is more important than the diffusion step. It is well known that in its crystalline form, Ce exhibits polymorphic transitions that start from rather low pressures due to its strongly correlated 4*f*-electrons and their delocalization with large density charges [28–31]; by varying the pressure, changes can be induced in the Ce–Ce interactions and *f*-electron delocalization, which enhances the electronic bonding, resulting in reduced Ce–Ce or Al–Ce interatomic distances. Recently, Sheng and co-workers [32] reported the observation of a pressure-induced transition between two distinct amorphous polymorphs in a $Ce_{55}Al_{45}$ metallic glass and demonstrated the existence of amorphous alloys that are compositionally identical, but with different thermodynamic, functional and rheological properties due to the different bonding and structural characteristics, which have been correlated with the polymorphic transitions of cerium.

In our work, the variation in the deposition conditions caused evident changes in the Al/Ce ratio which resulted in the amorphization of the aluminum phase; such amorphization is probably due to the polymorphic transitions of Ce, which also promoted changes in the short-range atomic structure of either the Ce–Ce or Ce–Al coordination numbers as it has been previously demonstrated [32]. This may explain the fact that no crystallization was observed in the samples deposited at $p_4P_{40}t_{300}$ and $p_4P_{120}t_{300}$. Then, in our work, the observed XRD results and HRTEM measurements indicate that depending on both the deposition parameters and Al/Ce ratio some kind of amorphous metallic glass with some crystallites embedded in the matrix were formed.

In order to analyze the surface morphology of the Al–Ce films, AFM images were obtained in different regions and areas of the samples. Fig. 6 (a–e) corresponds to the topography and three-dimensional images of the samples using SPIP 4.80 and Nanosurf easy scan 2.0 software. The effects on the surface morphology of the films as a consequence of the variations in the pressure and power can be observed in this figure. All the images show that the surface of the films was composed of equiaxial round domes homogeneously distributed with a mean grain size

Fig. 6. AFM topography and 3D mapping showing the growth morphologies of Al-Ce oxide films on Si varying Pressure (a) $p_{0.667}P_{200}t_{300}$, (b) $p_{1.333}P_{200}t_{300}$, (c) $p_4P_{200}t_{300}$ and AA6061 aluminum Alloy and Power, (d) $p_4P_{120}t_{300}$, and (e) $p_4P_{40}t_{300}$.

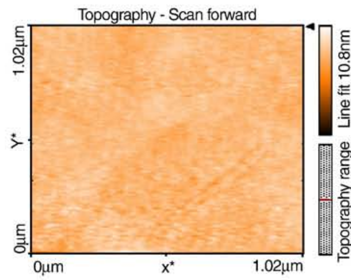
Topography - Scan forward
1.02µm
Y*
0µm
0µm
x*
1.02µm
Line fit 10.8nm
Topography range

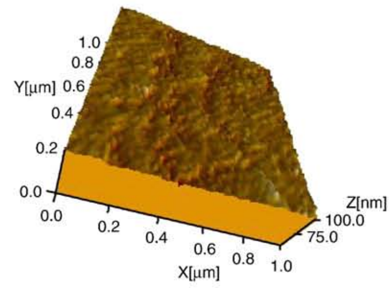
Y[µm]
X[µm]
Z[nm]
100.0
75.0
(a)

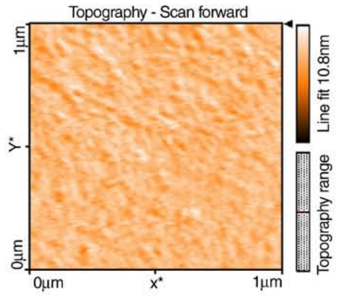
Topography - Scan forward
1µm
Y*
0µm
0µm
x*
1µm
Line fit 10.8nm
Topography range

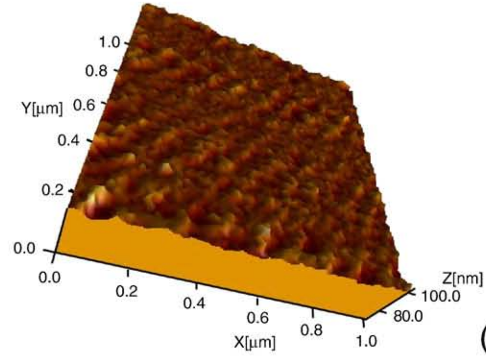
Y[µm]
X[µm]
Z[nm]
100.0
80.0
(b)

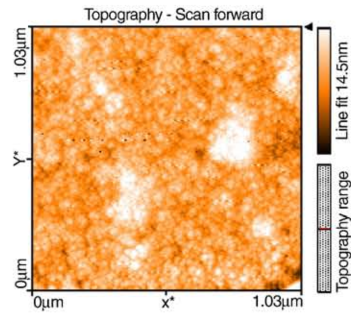
Topography - Scan forward
1.03µm
Y*
0µm
0µm
x*
1.03µm
Line fit 14.5nm
Topography range

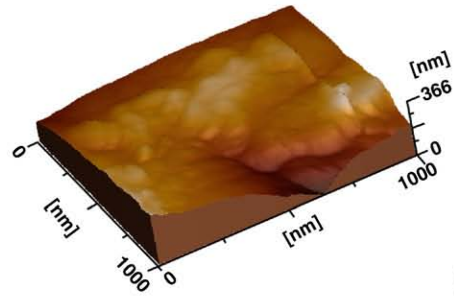
[nm]
366
0
1000
[nm]
[nm]
(c)

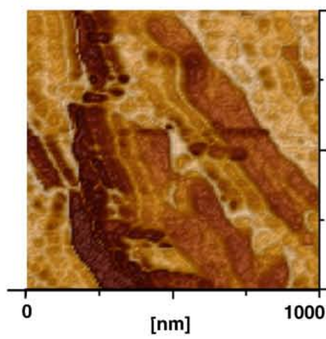
1000
[nm]
0
0
[nm]
1000

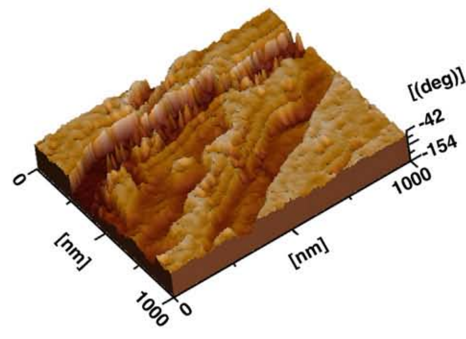
[(deg)]
-42
-154
1000
[nm]
[nm]
(d)

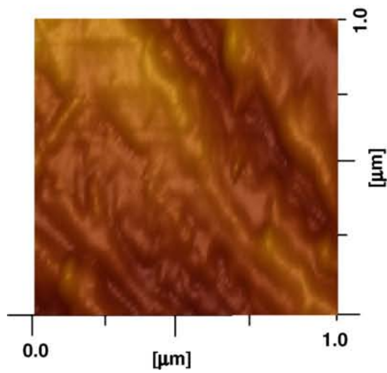
1.0
[µm]
0.0
[µm]
1.0

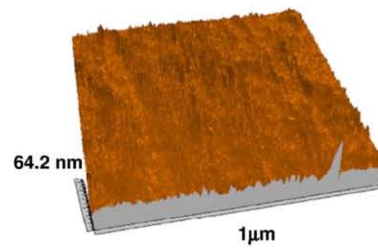
64.2 nm
1µm
(e)

increasing with the power at 4 Pa; however, at low power, the surface of the films was finer with wider and smoother domes. The mean particle size varies from 12 to 80 nm for the samples at 40 W and 200 W, respectively. The average roughness of the root mean square (rms) also increases with the supplied energy. The increase in the rms surface roughness can be related to a larger grain, which results when the power is increased. On the other hand, the effect exerted by pressure also caused an important increase in the deposition rate and morphology in the samples; in fact, it seems to be the major factor influencing the characteristics of the film growth. Such increases are also noticeable in Table 1 and in the roughness of the film, which ranged from 0.576 to 2.23 nm for the samples at $p_{0.667}P_{200}t_{300}$ and $p_4P_{280}t_{300}$.

Fig. 7(a–f) shows SEM micrographs of two selected surfaces at $p_4P_{200}t_{300}$ and $p_{0.667}P_{200}t_{300}$ as a reference of sputtered films on AA6061 aluminum alloy. To observe a contrast in the surface topographies, the samples are shown at different magnifications (2000×, 16,000× and 25,000×). The corresponding thicknesses of these samples can also be observed in these figures. In general, all the as-deposited sputtered films displayed a uniform, crack-free, densely packed surface with small pores and smoother domes covering the substrate uniformly. These films were grown with clusters of nanosized Al–Ce particles (Fig. 7(a–b) and (d–e). It is known that by changing the power or pressure, the sputter rate of the target changes results in differential deposition rates [33]. Moreover, in this case, microstructural variations were also observed at the different operating conditions: the particle size varied from ~15 to 80 nm as both the power and pressure were increased (fine to coarse grain size), and the thicknesses varied in the range of ~100 to 1200 nm depending on the experimental conditions (Fig. 7f and c, respectively). At these conditions, surface defects are not observable, which suggests that defects are only on the substrate surface.

The results are in good agreement with the profilometry results and AFM observations. The roughness increase promoted by the working pressure and power may be associated with two causes. Firstly, at low pressures the target voltage was the highest and the current was very low, the sputter rate was lower and as a consequence the films were thinner. This reduced growth rate induced low coarsening of the columns. In fact, the surface morphology of these thin films clearly resembled the coarse array of parallel polishing lines from the substrate, indicating that the islands formed by the growing films were still smaller than the polishing line spacing. Secondly, it has been demonstrated that at lower pressure, the ions experience fewer collisions during the transition and thus hit the film surface with more energy, producing a smoothening effect [34]. In addition, a less disperse ion flux is normally associated with a decrease in self-shadowing effects

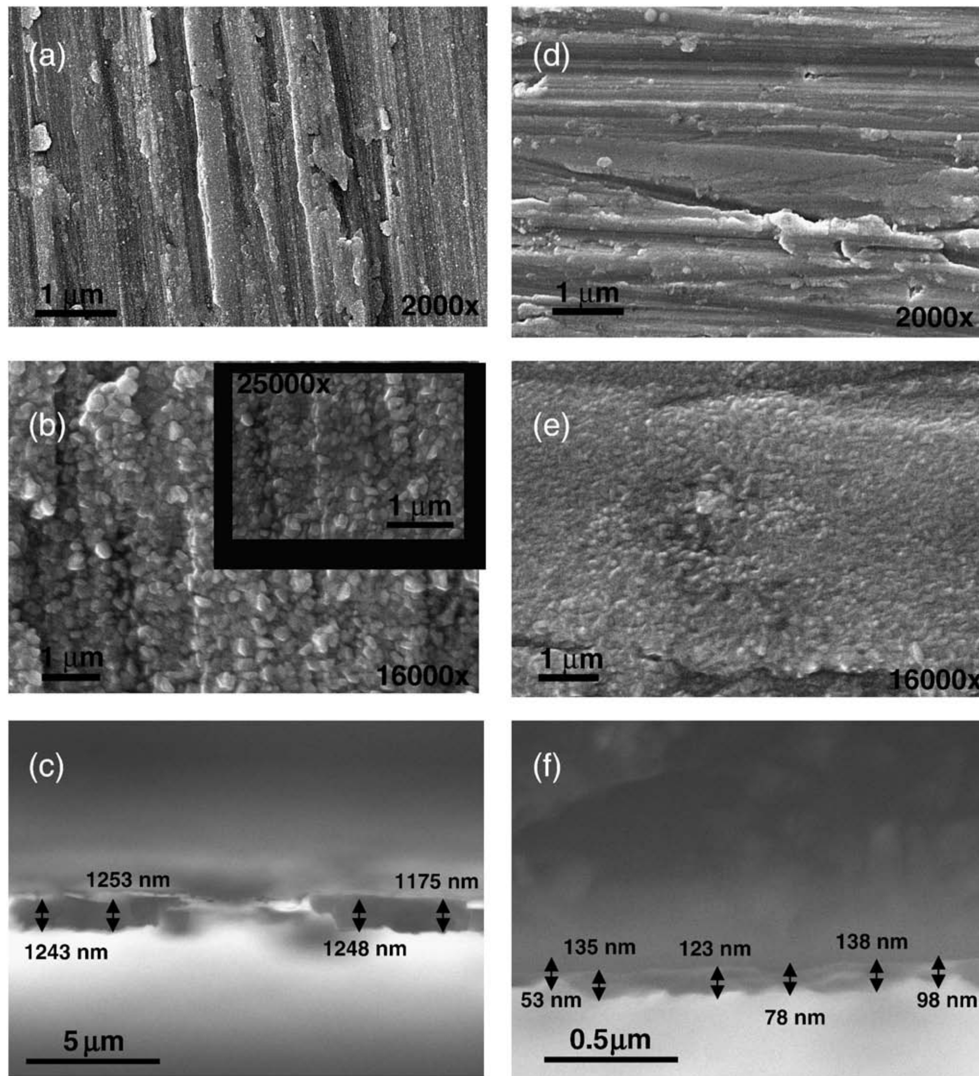

Fig. 7. SEM images showing the morphology at different magnifications (2000×, 16000× and 25000×) and thickness of two selected samples deposited on AA6061 aluminum alloy (a–c) $p_4P_{200}t_{300}$ and (d–f) $p_{0.667}P_{200}t_{300}$.

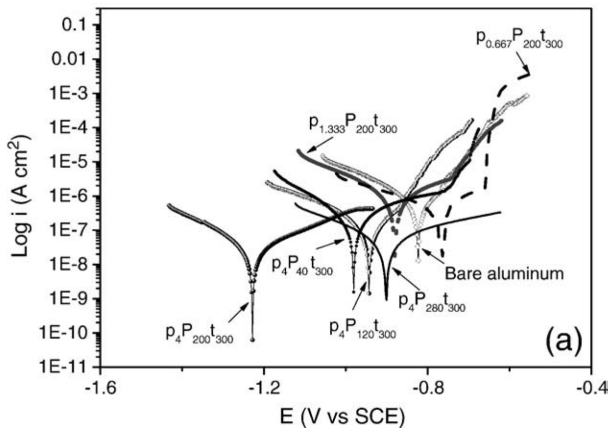

Fig. 8. Tafel plots of untreated and coated AA 6061 aluminum alloy samples after 24 h of immersion in a 3.5 wt.% NaCl aqueous solution.

and less surface roughening [35]. Finally, considering that the deposition time and Al–Ce ratio in the target were fixed, the variation in the morphology and microstructure was a direct consequence of the variation in the voltage–current characteristics during deposition as a consequence of the deposition parameters (power and pressure), which is in good agreement with previous studies [36]. The grain size was increased by increasing the power, which suggests a better organization of the deposited atoms in larger grains and a substantial reduction in the grain boundaries [37].

3.3. Electrochemical measurements

The electrochemical behavior of the treated Al alloy was studied by examining the Tafel plots obtained in a 3.5 wt.% NaCl aqueous solution, and their curves are reported in Fig. 8. The measurements were recorded for all the samples after 24 h of free corrosion potential in order to simulate a severe Cl^- ion attack. By comparing the coatings at the different experimental conditions with the bare sample, it can be seen that, except for the $p_{0.667}P_{200}t_{300}$, the samples show a negative displacement without any tendency. This trend is characteristic of cathodic inhibition [38]. The cathodic curves are slightly affected by the presence of the coatings, while the anodic curves for bare aluminum are characterized by an active behavior that shows intense activity in this potential region. For the samples coated at low pressure and power ($p_{0.667}P_{200}t_{300}$, $p_{1.333}P_{200}t_{300}$ and $p_4P_{40}t_{300}$), a passive region with a well-defined pitting potential is observed. This value is close to the open circuit potential (OCP). By comparing these coating samples, it can be

Fig. 9. Impedance spectra of the bare aluminum and coated samples.

found that the shape of the curves is similar, but the pitting potential is displaced without any clear trend. On the contrary, by increasing the power and pressure ($p_4P_{120}t_{300}$, $p_4P_{200}t_{300}$ and $p_4P_{280}t_{300}$), the OCP gradually becomes more negative and the anodic curve starts to present a passive region. It must be emphasized that the polarization curves were obtained after 24 h of immersion, pointing towards an effective protection of the alloy substrate by the presence of the Al–Ce coating under these experimental conditions. This behavior can be correlated with the increase in the cerium quantity in the film. On the other hand, a slight displacement in the i_{corr} toward lower values is also observable for almost all the coatings. However, such diminution, in the best cases, was around one order of magnitude.

Electrochemical impedance spectroscopy (EIS) was used to assess the evolution of corrosion after 24 h of immersion in the aggressive medium. EIS provided useful information on the corrosion processes in the PVD coated samples when exposed to an aggressive environment [39]. Fig. 9(a–c) presents the Nyquist and Bode diagrams of the coated and uncoated samples. The Nyquist plots in Fig. 9a show that the diagrams displayed one depressed semicircle which is attributed to the protective layer and a diffusion tail in the low frequency range. This tail can be correlated with the electrolyte diffusion throughout the film, surface inhomogeneities (defects or domes) of the coatings and would correspond to the existence of a slope at low frequencies in the Bode modulus diagram (Fig. 9c); this slope increases with the coatings, indicating that the oxidant species presented certain difficulties to reach the substrate and take part in the cathodic reaction. Due to the fact that the Bode angle diagram is extended in a wide frequency range (~10^4–10^{-1} Hz), it could be found that the maximum is actually a consequence of the overlapping of two processes (Fig. 9b). As it can be seen in the figure, the overlapping of the two processes is higher for the $p_4P_{200}t_{300}$ samples than that presented by bare aluminum. The first process at higher-medium frequencies is commonly associated with the film resistance, while the time constant at medium-low frequencies is usually related to the charge transfer resistance. Frequencies lower than 10^{-1} Hz, which are usually correlated with the corrosion phenomenon in the solution, are related to an exfoliation, intergranular or pitting corrosion [40,41]. Then, the first process of the time constant centered at 10^2 Hz is related to the outermost Al–Ce film; and the observed depressed semicircles can be attributed to the geometrical parameters of the microstructure, which reproduces the surface topography of the alloy [42]. In the case of bare aluminum, the depressed arc is a consequence of the thermo-mechanical treatment applied to the alloy, which changed the size of the precipitates protruding from the oxide layer and increased the surface roughness [15,43].

From these diagrams, no significant variations in the low frequency impedance are seen, except an important increase in the polarization resistance (Rp) values. The Rp values were graphically estimated from the EIS diagrams as $Rp = |Z(j\omega)|_{\omega\to 0} - |Z(j\omega)|_{\omega\to\infty}$ [44,45]. The corresponding Rp of the substrate and the coatings showed that the bare aluminum presented the lowest polarization resistance (4.956 kΩ cm^2), while the coated samples presented higher corrosion resistance than the bare aluminium. Rp values up to 138.4 kΩ cm^2 were obtained with coated samples at $p_4P_{200}t_{300}$; in accordance with the traditional interpretation that associates higher values of impedance with a higher resistance to corrosion. The data obtained with the coated samples at the experimental conditions, $p_4P_{200}t_{300}$ and $p_4P_{280}t_{300}$, indicated that the coated AA6061 aluminum alloy presented higher corrosion resistance than the bare aluminum. The elemental analysis of these films revealed that the composition of these films was Al (62.27 wt.%), Ce (35.54 wt.%), O (2.95 wt.%) and Al (66.54 wt.%), Ce (31.41 wt.%), O (2.19 wt.%), respectively. As it was stated above, these oxide samples formed under environmental conditions are composed of an amorphous phase with some crystallites embedded in the matrix in combination with some surface defects caused by the operating conditions and the inner Al-oxide layer on the alloy substrate. The high cerium content (Al/Ce ratio) and structure of the films (metallic glass) may explain the enhancement of the electrochemical behaviour in comparison with the counterparts.

After applying the protective coating, the electrochemical results display: i) the inhibition of the cathodic and anodic reactions; and ii) increased impedance values, which are usually related to a decreased active area. The Al–Ce oxides in the inner layer of the passive films function as a barrier layer. Additionally, during immersion, the characteristic time constant at low frequencies, which is assigned to the pitted Al oxide layer, was not observed. This situation suggests that these experimental facts are promising for the enhancement of the resistance to pitting corrosion in this aluminum alloy. Finally, the role of the cerium content is not only to delay corrosion in the material, but depending of the experimental conditions, to avoid the crystallization of the alumina film, which could be interesting in some industrial applications. In this case, the minimum cerium content to reduce the corrosion process is about 30 wt.% in the film, while to totally avoid the crystallization of the film, the cerium quantity should be close to 2 wt.%; although it depends on the operating conditions.

4. Conclusions

The effects of pressure and power of the DC sputtering system on the deposition rate, structure and protection against corrosion of sputtered Al–Ce films has been investigated using Si (111) and AA6061 aluminum alloy as substrates. The results indicated that the chosen parameters (power and pressure) have a high influence on the Al/Ce ratio, which seems to be a consequence of the significant difference between the sputtering yield of Ce and Al. Cerium and Aluminum oxide compounds were formed once that samples were exposed to the atmosphere due to the well known reactivity of both elements under environmental conditions, but not as a consequence of contamination in the sputtering chamber; the oxygen contents in the film varied from 8 to 40%, according to RBS. Depending on the operating conditions (adjusting power and pressure), films with very fine grained nanocrystals, “metallic glasses” or amorphous films can be obtained as a consequence of the polymorphic transitions of cerium. The metallic glass films were mainly composed of small crystallites of intermetallic compounds such as $CeAlO_3$, Al_4Ce, Al_3Ce and Cerium oxide compounds (+3 and +4) embedded in an amorphous matrix of alumina.

In addition, both power and pressure conditioned the mean particle size (~12–80 nm), surface defects, deposition rate, thickness (~100–1200 nm) and roughness (~0.576–2.3 nm) of the films. The substrate does not seem to have any influence on the crystallinity or orientation during the growth of the film.

The Al/Ce ratio in the film had a significant influence on the preliminary corrosion behavior; higher Cerium contents were more effective against corrosion than those with low Ce quantities. These electrochemical results displayed two important aspects: i) inhibition of the cathodic and anodic reactions; and ii) increased impedance values, usually related to a decreased active area. The films that displayed the most relevant electrochemical performance under the experimental conditions are: $p_4P_{200}t_{300}$ and $p_4P_{280}t_{300}$ whose elemental compositions are Al (62.27 wt.%), Ce (35.54 wt.%), O (2.19 wt.%) and Al (66.54 wt.%), Ce (31.41 wt.%), O (2.95 wt.%), respectively. Studies of the mechanism and significance of the amorphization as well as a detailed electrochemical characterization are in progress.

Acknowledgements

This study has been financially supported by CONACYT (project number 61354) and the Instituto Politécnico Nacional (projects Number SIP-2009-0561, 2009-0499) and SNI-CONACYT. The authors would like to thank Beatriz Brachetti Sibaja, Lázaro Huerta and Mr. Javier Zapata Torres for their technical support; and Instituto de Física de la UNAM for the RBS measurements.

References

[1] B.R.W. Hinton, D.R. Arnott, N.E. Ryan, Mater. Forum 9 (1986) 162.
[2] A. Pardo, M.C. Merino, R. Arrabal, F. Viejo, J.A. Muñoz, Appl. Surf. Sci. 253 (2007) 3334.
[3] H. Ardelean, C. Fiaud, P. Marcus, Mater. Corros. 52 (2001) 889.
[4] A.J. Davenport, H.S. Isaacs, M.W. Kendig, Corros. Sci. 32 (1991) 653.
[5] Y. Xiong, K. Yamaji, N. Sakai, H. Negishi, T. Horita, H. Yokohama, J. Electrochem. Soc. 148 (2001) EA489.
[6] Y. Wang, Z. Wang, Y. Yang, W. Chen , Intermetallics 16 (2008) 682.
[7] W. Pinc, S. Geng, M. O'Keefe, W. Fahrenholtz, T. O'Keefe, Appl. Surf. Sci. 255 (2009) 4061.
[8] M. Teng, L. Luo, X. Yang, Microporous Mesoporous Mater. 119 (2009) 158.
[9] T.J. Haley, J. Pharm Sci. 54 (1965) 633.
[10] X. Li, S. Deng, H. Fu, G. Mu, Corros. Sci. 50 (2008) 3599.
[11] A. Salam Hamdy, Materials Letters 60 (2006) 2633.
[12] Y. Huang, H. Shih, H. Huang, J. Daugherty, S. Wu, S. Ramanathan, C. Chang, F. Mansfeld, Corros. Sci. 50 (2008) 3569.
[13] X. Yu, C. Cao, Thin Solid Films 423 (2003) 252.
[14] J. Hu, S. Tang, Z. Zhang, Corros. Sci. 50 (2008) 3185.
[15] A. Conde, M.A. Arenas, A. de Frutos, J. de Damborenea, Electrochim. Acta 53 (2008) 7760.
[16] A. de Frutos, M.A. Arenas, Y. Liu, P. Skeldon, G.E. Thompson, J. de Damborenea, A. Conde, Surf. Coat. Technol. 202 (2008) 3797.
[17] B. Enders, S. Krau, K. Kaba, G.K. Wolf, Surf. Coat. Technol. 74–75 (1995) 959.
[18] E.V. Parfenov, A.L. Yerokhin, A. Matthews, Thin solid films 516 (2007) 428.
[19] P.J. Kelly, R.D. Arnell, Vacuum 56 (2000) 159.
[20] L. Cunha, M. Andritschky, K. Pischow, Z. Wang, Thin Solid Films 355–356 (1999) 465.
[21] J.J. Olaya, S.E. Rodil, S. Muhl, E. Sánchez, Thin Solid Films 474 (2005) 119.
[22] F.B. Rivera, Y.B. Jhonson, J.M. O'Keefe, G.W. Fahrenholtz, Surf. Coat. Technol. 176 (2004) 349.
[23] Standard Practice for: Preparing, Cleaning, and Evaluating Corrosion Test Specimens ASTM G1-03, American Society for Testing and Materials, West Conshohocken, PA, (2003).
[24] J.P. Biersack, W. Eckstein, Appl. Phys. A 34 (1984) 73.
[25] J.F. Ziegler, J.P. Biersack, U. Littmark, The Stopping and Range of Ions in Solids, Pergamon Press, New York, 2009.
[26] J. Musil, J. Vlcek, Surf. Coat. Technol. 142–144 (2001) 557.
[27] J.A. Thornton, in: R.F. Bunshah (Ed.), Deposition technologies for films and coatings, Noyes Publications, Park Ridge, NJ, 1982, p. 214.
[28] J.A. Thornton, J. Vac. Sci. Technol. A 4 (1986) 3059.
[29] A. Svane, et al., Int. J. Quant. Chem. 77 (2000) 799.
[30] A.B. Shick, W.E. Pickett, A.I. Liechtenstein, J. Electron Spectrosc. Relat. Phenom. 114 (2001) 753.
[31] K.A. Gschneider Jr, L.R. Eyring (Eds.), Handbook on the Physics and Chemistry of Rare Earths, 1978, North-Holland, Amsterdam.
[32] H.W. Sheng, H.Z. Liu, Y.Q. Cheng, J. Wen, P.L. Lee, W.K. Luo, S.D. Shastri, E. Ma, Lett., Nat. Mater. 6 (2007) 192.
[33] M. Ohring, The Materials Science of Thin Films, Academic Press, San Diego, CA, 1991.
[34] U. Figueroa, O. Salas, J. Oseguera, Surf. Coat. Technol. 200 (2005) 1768.
[35] D.L. Smith, Thin Film Deposition: Principles and Practice, Mc Graw Hill, Boston, MA, 1995, p. 165.
[36] P.J. Kelly, R.D. Arnell, J. Vac. Sci. Technol., A, Vac. Surf. Films 16 (1998) 2858.
[37] J.J. Olaya, S.E. Rodil, S. Muhl, L. Huerta, Surf. Coat. Technol. 200 (2006) 5743.
[38] M. Bethencourt, F.J. Botana, M.J. Cano, M. Marcos, Appl. Surf. Sci. 238 (2004) 278.
[39] C. Liu, Q. Bi, H. Siéguele, A. Leyland, A. Matthews, J. Vac. Sci. Technol. A A20 (2002) 772.
[40] A. Conde, J.J. de Damborenea, Rev. Metal. 34 (1998) 75.
[41] A. Conde, J.J. de Damborenea, Mater. Corros. 50 (1999) 447.
[42] Z. Lukács, J. Electroanal. Chem. 432 (1997) 79.
[43] P.L. Cabot, J. Appl. Electrochem. 25 (1995) 180.
[44] A.J. Bard, L.R. Faulanker, Electrochemical Methods, vol. 16, Wiley, New York, 1987.
[45] S.C. Chung, S.L. Sung, C.C. Hsien, H.C. Shih, J. Appl. Electrochem. 30 (2000) 607.